energies

MDPI

Article

Experimental Investigation of Coupled Transport Mechanisms in a PEM Based Thermoelectric Energy Converter

Maike Willke [1,*], Nils-Eric Rahm [2] and Stephan Kabelac [1]

[1] Institute of Thermodynamics, Leibniz University Hannover, 30167 Hannover, Germany; kabelac@ift.uni-hannover.de
[2] Institute of Electric Power Systems, Leibniz University Hannover, 30167 Hannover, Germany; rahm@ifes.uni-hannover.de
* Correspondence: willke@ift.uni-hannover.de; Tel.: +49-511-762-13151

Abstract: Thermoelectric energy converters based on galvanic cells (TGC) offer the possibility of direct conversion of low-temperature waste heat into electrical energy and could therefore be a promising approach for an increase in the overall efficiency of energy conversion. Due to an externally applied heat source, a temperature gradient across the electrolyte is induced, leading to a gradient in the chemical potential of the species and an electrical potential difference between the electrodes. The aim of approaching an internal equilibrium state leads to various coupled molecular transport mechanisms taking place in the electrolyte, impacting the open circuit voltage (OCV) and the performance of the TGC. By applying the theory of non-equilibrium thermodynamics (NET) to describe these coupled processes, the interactions that occur can be characterized in more detail. In this work, a polymer electrolyte membrane (PEM)-based TGC with two H_2/H_2O electrodes of different temperatures and gas compositions is experimentally investigated. By controlling the gradients in temperature and concentration, different impacts on the resulting OCV can be identified. In addition, we present the measured coupling coefficient, representing the singular relation between the transport of the hydrogen ions inside the membrane and the electrical potential difference between the electrodes for a wide variety of working conditions.

Keywords: thermogalvanic cell; polymer electrolyte membrane; energy conversion; non-equilibrium thermodynamics; coupled molecular transport mechanisms

Citation: Willke, M.; Rahm, N.-E.; Kabelac, S. Experimental Investigation of Coupled Transport Mechanisms in a PEM Based Thermoelectric Energy Converter. *Energies* **2023**, *16*, 5434. https://doi.org/10.3390/en16145434

Academic Editor: Felix Barreras

Received: 2 June 2023
Revised: 18 June 2023
Accepted: 12 July 2023
Published: 17 July 2023

1. Introduction

As a byproduct of many technical processes, low-temperature heat is widely available in large quantities, but it is often dumped into the environment as waste heat. A more efficient overall energy conversion is possible by heat harvesting, and thus, the resource usage for the energy supply can be reduced [1,2]. A promising approach in this context is the direct conversion of low temperature waste heat into electrical energy using a thermoelectric generator (TEG). There are different working principles available, such as semiconductor based thermoelectric cells (TEC) or thermogalvanic cells (TGC). While the first are commonly used at higher overall temperatures and temperature differences due to their increasing efficiency and economic added value, the latter can convert low-grade waste heat ($T < 100$ °C) into electricity [3]. A TGC consists of an electrolyte, which contains a redox couple, and two identical electrodes with a non-zero Seebeck thermoelectric coefficient connected to an external electric circuit. Due to the temperature-dependent redox reaction, an applied temperature difference between the electrodes provides an electromotive force (EMF), which induces the anodic oxidation reaction associated with the cathodic reduction reaction of the redox couple. There are different concepts of TGCs available: those that contain all the reactants in the electrolyte, making a continuous operation possible as all species are transported through the electrolyte [4–6], and others that need the reactants

provided externally at both electrodes [7–9]. For steady operation of the latter, the reactants must either be recirculated or the electrodes sequentially heated and cooled [10]. In addition to these different concepts, TGCs also vary in redox couples and electrolytes, which is well summarized in [11]. Due to its increasing availability and without any climate impact, the use of green hydrogen as a reactant in TGC shows great potential, which has already been proven in other thermoelectric energy converters [12–14]. As the amount of low-temperature waste heat increased continuously over the past years, the TGC could find application in several fields, such as stable devices (energy source: i.e., solar radiation, geothermal sources, household appliances) or wearable and portable devices (energy source: i.e., human body, automobiles) [15].

In this work, a TGC consisting of a solid polymer membrane as the electrolyte (PEM) and two humidified hydrogen gas electrodes of different temperatures is considered, as presented in [10,16,17] (see Figure 1). An EMF is generated due to the temperature gradient between the electrodes. When load is applied to the cell, the hydrogen oxidation reaction occurs at the anodic electrode, whereby H^+ ions and electrons are released:

$$H_2 \rightarrow 2{\cdot}H^+ + 2{\cdot}e^- \tag{1}$$

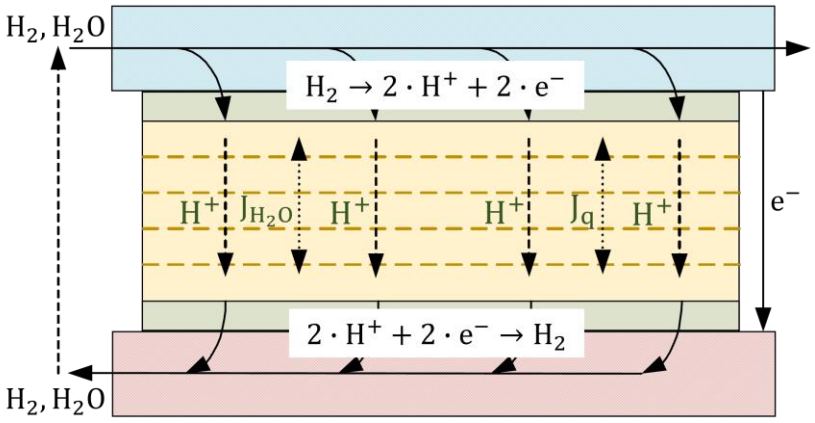

Figure 1. Schematic of a PEM-based thermogalvanic cell, including the heat flux J_q, the water flux J_{H_2O} and the proton flux H^+.

While the ions are transported through the electrolyte, the electrons flow via an external electric circuit to the cathodic electrode, where the reduction reaction takes place and hydrogen is formed again:

$$2{\cdot}H^+ + 2{\cdot}e^- \rightarrow H_2. \tag{2}$$

Hence, there is no net consumption of hydrogen in the overall process.

The concept of the TGC presented in this work shows great potential in terms of quick feasibility and availability due to the use of common PEM fuel cell (FC) components in the cell setup and the self-supplied hydrogen electrodes, which can easily be obtained. However, similar PEM-based TGCs investigated in previous studies show comparably low open circuit voltages (OCV) ($U_{cell,0,max} < 80$ mV) and maximum power densities not exceeding 0.45 W/m^2 [10,17]. Prior to the commercial use of such TGC, its performance, including the OCV, needs to be improved and internal losses minimized.

The overall reaction as well as the rising OCV strongly depend on the working conditions of the TGC and the coupled transport mechanisms taking place in its electrolyte. By analyzing these coupled transport mechanisms, the local entropy production rate as well as the internal losses can be characterized in more detail according to the theory of Non-Equilibrium Thermodynamics (NET). The experimental investigation of different impacts on the OCV of the PEM-based TGC is the subject of this work.

2. Theoretical Background

Based upon the condition of an electrochemical equilibrium under open circuit conditions inside the TGC, the electrical cell potential as follows [18]:

$$U_{\text{cell},0} = \phi^{\text{c}} - \phi^{\text{a}} = \Delta\phi^{\text{c}} - \Delta\phi^{\text{a}} + \Delta\phi^{\text{m}} \tag{3}$$

with

$$\begin{aligned} \Delta\phi^{\text{a}} = (\phi^{\text{a}} - \phi^{\text{ma}}) \quad &= -\tfrac{1}{2\cdot F}\cdot\mu_{\text{H}_2}(T^{\text{a}}, p^{\text{a}}) \\ &= -\left[\frac{G^{\theta}_{\text{m,0,H}_2}(T^{\text{a}})}{2\cdot F} + \frac{R_{\text{m}}\cdot T^{\text{a}}}{2\cdot F}\cdot\ln\left(\frac{f^{\text{a}}_{\text{H}_2}\left(T^{\text{a}},\, x^{\text{a}}_{\text{H}_2}\right)}{p^{\theta}}\right)\right] \end{aligned} \tag{4}$$

$$\begin{aligned} \Delta\phi^{\text{c}} = (\phi^{\text{c}} - \phi^{\text{mc}}) \quad &= -\tfrac{1}{2\cdot F}\cdot\mu_{\text{H}_2}(T^{\text{c}}, p^{\text{c}}) \\ &= -\left[\frac{G^{\theta}_{\text{m,0,H}_2}(T^{\text{c}})}{2\cdot F} + \frac{R_{\text{m}}\cdot T^{\text{c}}}{2\cdot F}\cdot\ln\left(\frac{f^{\text{c}}_{\text{H}_2}\left(T^{\text{c}},\, x^{\text{c}}_{\text{H}_2}\right)}{p^{\theta}}\right)\right] \end{aligned} \tag{5}$$

leading to its Nernst equation:

$$\begin{aligned} U^{\theta}_{\text{cell},0} = \text{OCV} = \quad & \frac{G^{\theta}_{\text{m,0,H}_2}(T^{\text{a}})}{2\cdot F} - \frac{G^{\theta}_{\text{m,0,H}_2}(T^{\text{c}})}{2\cdot F} + \frac{R_{\text{m}}\cdot T^{\text{a}}}{2\cdot F}\cdot\ln\left(\frac{f^{\text{a}}_{\text{H}_2}\left(T^{\text{a}},\, x^{\text{a}}_{\text{H}_2}\right)}{p^{\theta}}\right) \\ & - \frac{R_{\text{m}}\cdot T^{\text{c}}}{2\cdot F}\cdot\ln\left(\frac{f^{\text{c}}_{\text{H}_2}\left(T^{\text{c}},\, x^{\text{c}}_{\text{H}_2}\right)}{p^{\theta}}\right) + \Delta\phi^{\text{m}}. \end{aligned} \tag{6}$$

One can see that the OCV of the TGC is impacted by the electrode temperatures, the gas composition of the supplied gas mixtures, and a gradient in the electrical potential across the membrane $\Delta\phi^{\text{m}}$. The latter is impacted by the resulting coupled processes in the membrane due to the interactions of the present forces and fluxes. These processes can be described and analyzed by means of the Non-Equilibrium Thermodynamics (NET) established by L. Onsager [19,20]. In terms of the NET, the volumetric entropy production rate results from the sum of all existing fluxes and forces in a given system as follows:

$$\dot{s}_{\text{v,irr}} = \sum_{i}^{n} J_i \cdot X_j. \tag{7}$$

Any one-dimensional flux J_i occurring in a system arises from a combination of all existing forces X_j and their related coupling coefficients L_{ij}. This coupling can be sufficiently approximated to be a linear function [21]:

$$J_i = \sum_{i}^{n} L_{ij} \cdot X_j. \tag{8}$$

By applying this theory to the PEM-based TGC with two H_2/H_2O electrodes of different gas compositions and temperatures, the resulting fluxes of water, hydrogen ions, and heat inside the electrolyte can be described as:

$$J'_{\text{q}} = -L_{\text{qq}}\left(\frac{1}{T^2}\frac{dT}{dx}\right) + L_{\text{qw}}\left(-\frac{1}{T}\frac{d\mu}{dx}\right) + L_{\text{q}\phi}\left(-\frac{1}{T}\frac{d\phi}{dx}\right), \tag{9}$$

$$J_{\text{w}} = -L_{\text{wq}}\left(\frac{1}{T^2}\frac{dT}{dx}\right) + L_{\text{ww}}\left(-\frac{1}{T}\frac{d\mu}{dx}\right) + L_{\text{w}\phi}\left(-\frac{1}{T}\frac{d\phi}{dx}\right), \tag{10}$$

$$j = -L_{\phi\text{q}}\left(\frac{1}{T^2}\frac{dT}{dx}\right) + L_{\phi\text{w}}\left(-\frac{1}{T}\frac{d\mu}{dx}\right) + L_{\phi\phi}\left(-\frac{1}{T}\frac{d\phi}{dx}\right). \tag{11}$$

When considering open circuit conditions ($j = 0$) and assuming constant coefficients throughout the electrolyte membrane, one can express the electric potential difference across the electrolyte membrane by rearranging Equation (11) as:

$$\Delta\phi^{\mathrm{m}} = -\left(\frac{L_{\phi\mathrm{q}}}{L_{\phi\phi}}\cdot\frac{\Delta T^{\mathrm{m}}}{T^{\mathrm{m}}} + \frac{L_{\phi\mathrm{w}}}{L_{\phi\phi}}\cdot\Delta\mu^{\mathrm{w,m}}\right). \tag{12}$$

A common approach to describing the phenomenological coefficients impacting the OCV is to use classical transport coefficients [22,23]. The coefficient $L_{\phi\phi}$ represents the specific relation between the flux of hydrogen ions and the electrical potential difference across the membrane, i.e., when all other gradients of influence are zero. This relation can be expressed by the electric resistivity r^{m} or the ionic conductivity κ^{m}:

$$r^{\mathrm{m}} = \frac{1}{\kappa^{\mathrm{m}}} = \left(\frac{\frac{d\phi}{dx}}{j}\right)_{d\mu^{\mathrm{w,m}}=0,\ dT^{\mathrm{m}}=0} = \frac{T}{L_{\phi\phi}}. \tag{13}$$

Different methods for the determination of the electric resistivity of PEM depending on the temperature and/or water content can be found in the literature [24–26]. The most common and frequently used approximation in theoretical models is one introduced by Springer et al. [26]:

$$\kappa^{\mathrm{m}} = \frac{1}{r^{\mathrm{m}}} = (0.5139\cdot\lambda^{\mathrm{w}} - 0.326)\cdot\exp\left(1268\cdot\left(\frac{1}{303} - \frac{1}{T^{\mathrm{m}}}\right)\right). \tag{14}$$

An approach for $L_{\phi\mathrm{q}}$ and $L_{\phi\mathrm{w}}$ are the empirical water transference number $t^{\mathrm{w,m}}$ and Peltier coefficient π^{m} respectively [22,27], which are beyond the scope of this work but need to be identified in future research activities.

3. Experimental

3.1. Experimental Setup

The membrane electrode assembly (MEA) of the TGC used in this work is composed of a stacked layer of four plain membranes and two membranes coated with catalyst ink (Pt/C + ionomer, 0.3 mg Pt/cm^2) of the type Nafion$^{\mathrm{TM}}$ N117 ($d = 6 \times 183$ µm $= 1098$ µm) with a surface area of 25 cm^2. The membranes consist of a polytetrafluoroethylene backbone with various perfluorinated-vinyl-polyether side chains, which contain sulphonic acid end groups providing mechanical strength and protonic conductivity, respectively [28]. The stacking of membranes is required to increase the thermal resistance of the MEA and to ensure a temperature gradient of up to $\Delta T = 60$ K to be maintained. The MEA is surrounded by two SIGRACET® 28BC gas diffusion layers, which, together with a teflon foil for sealing purposes, are pressed between the monopolar plates using LEANCAT compression hardware, ensuring homogeneous pressure over the entire sample cell. The pressure on the active area of the TGC is held constant at 0.714 MPa. The stainless steel monopolar plates (X6DrNiTi 1810) have a serpentine flow field (FF) and through-holes, which are connected to LAUDA thermostats pumping temperature-controlled water for heating or cooling purposes through the plates. For the conditioning of the gas flow, a Controlled Evaporation Mixing (CEM) System by Bronkhorst is used for each electrode, which consists of a liquid flow controller, a gas mass flow controller (MFC), and an evaporation device. There is one MFC for hydrogen (purity 5.0) implemented on the cathodic site, and two MFCs are used on the anodic site, one for hydrogen (purity 5.0) and the other for nitrogen (purity 5.0). This gives the opportunity to set up a temperature gradient between the electrodes while suppressing the gradient in chemical potential of the water solved in the membrane and the partial pressure of the hydrogen, which also effects the open circuit voltage (see Equation (6)). The gas is humidified with deionized water ($\kappa < 1$ µS). Controllable heating wires are implemented in the tubes between the outlet of the CEM

and the inlet of the monopolar plates in order to avoid condensation of the water vapor in the gas stream. The schematic design of the test setup is shown in Figure 2.

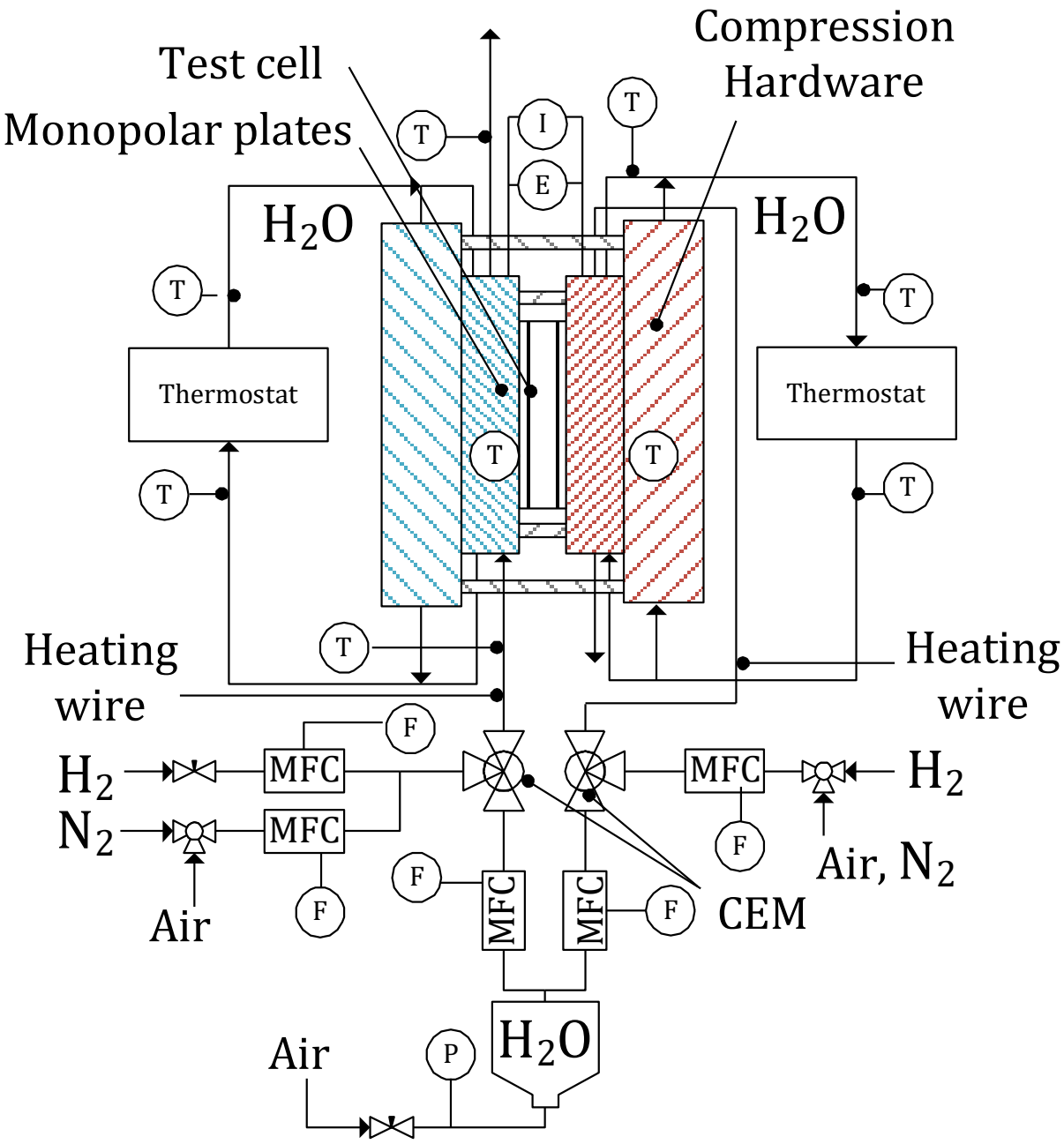

Figure 2. Schematic of test setup, including peripheric system and measuring points.

A picture of the actual experimental setup can be seen in Figure 3.

Different sensors monitor the temperature across the setup. To measure the temperature of the gas stream at the inlet and outlet of the plates, PT100 is used. Thermocouples type K detect the temperature of the monopolar plates, the heating wire, and the water temperature for heating and cooling the thermostats. Thermocouples of type T with a diameter of 0.25 mm are implemented inside the flow field to measure the temperature distribution inside the cell without impacting the cell's operation or internal processes. The location of the thermocouples inside the cell is shown in Figure 4.

Figure 3. Picture of the actual experimental setup.

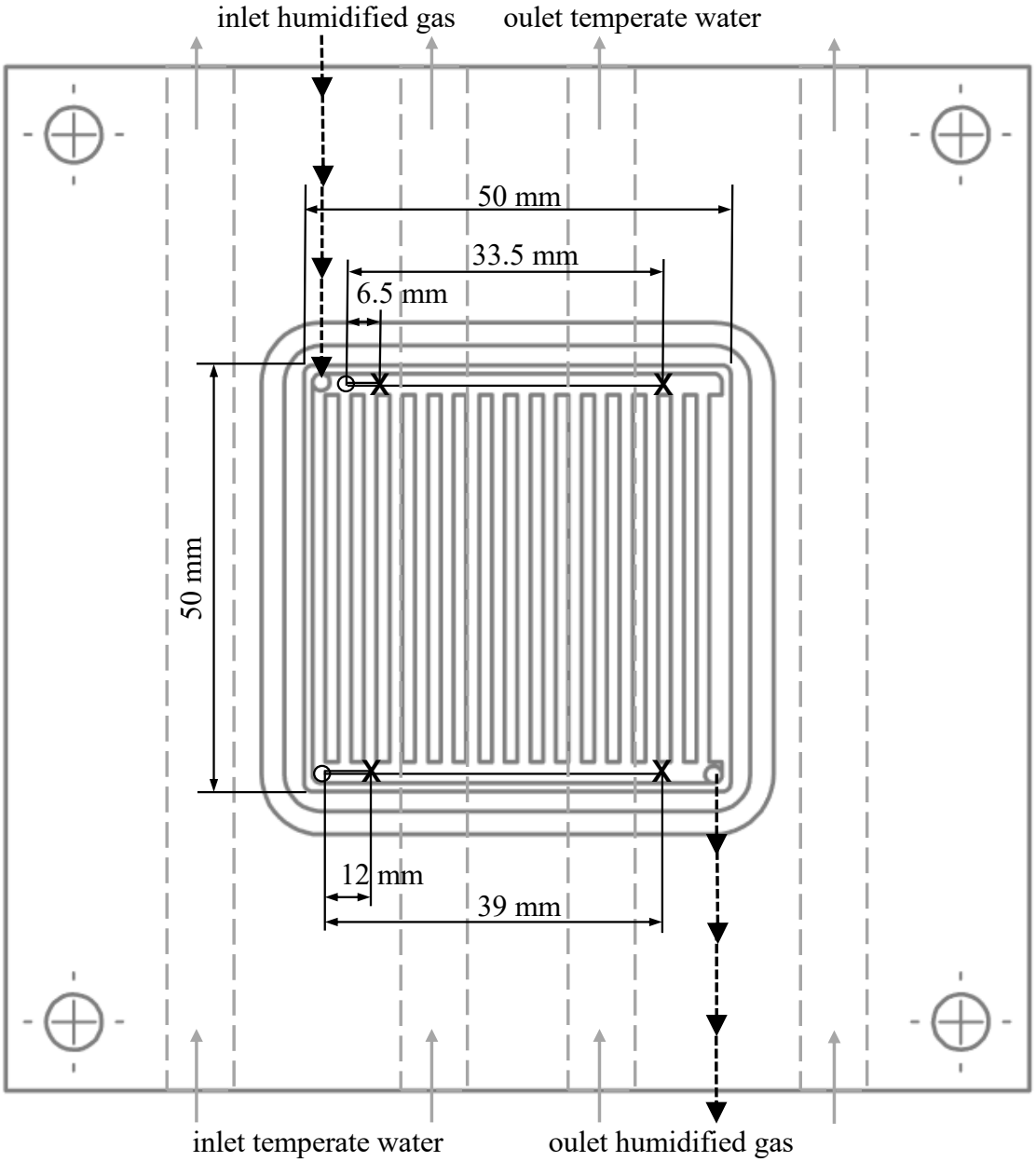

Figure 4. Monopolar plate with thermocouple positions in FF.

The cell voltage is measured with a NI9211 module from National Instruments. To determine internal cell resistances as well as the high frequency resistance (HFR) of the cell, which is needed to determine the coefficient $L_{\phi\phi}$, an electrochemical impedance device, the ModuLab XM CHAS 08 by SOLARTRON ANALYTICAL, is used. Figure 5 shows the possible range of measurement of our test setup in terms of electrode temperatures and the chemical potential of the water. The limit for the maximum temperature is set by the characteristics of the Nafion^{TM} membrane, which should not exceed 85 °C due to degradation reasons [29]. The range of the chemical potential of the water depends on the valid relative humidity of the gas stream, which affects the membrane water content. The minimum acceptable relative humidity is set to 5% to ensure hydrogen ion transport through the membrane, while the maximum relative humidity should not exceed 95% to avoid condensation of the water at potential cold spots in the setup [30].

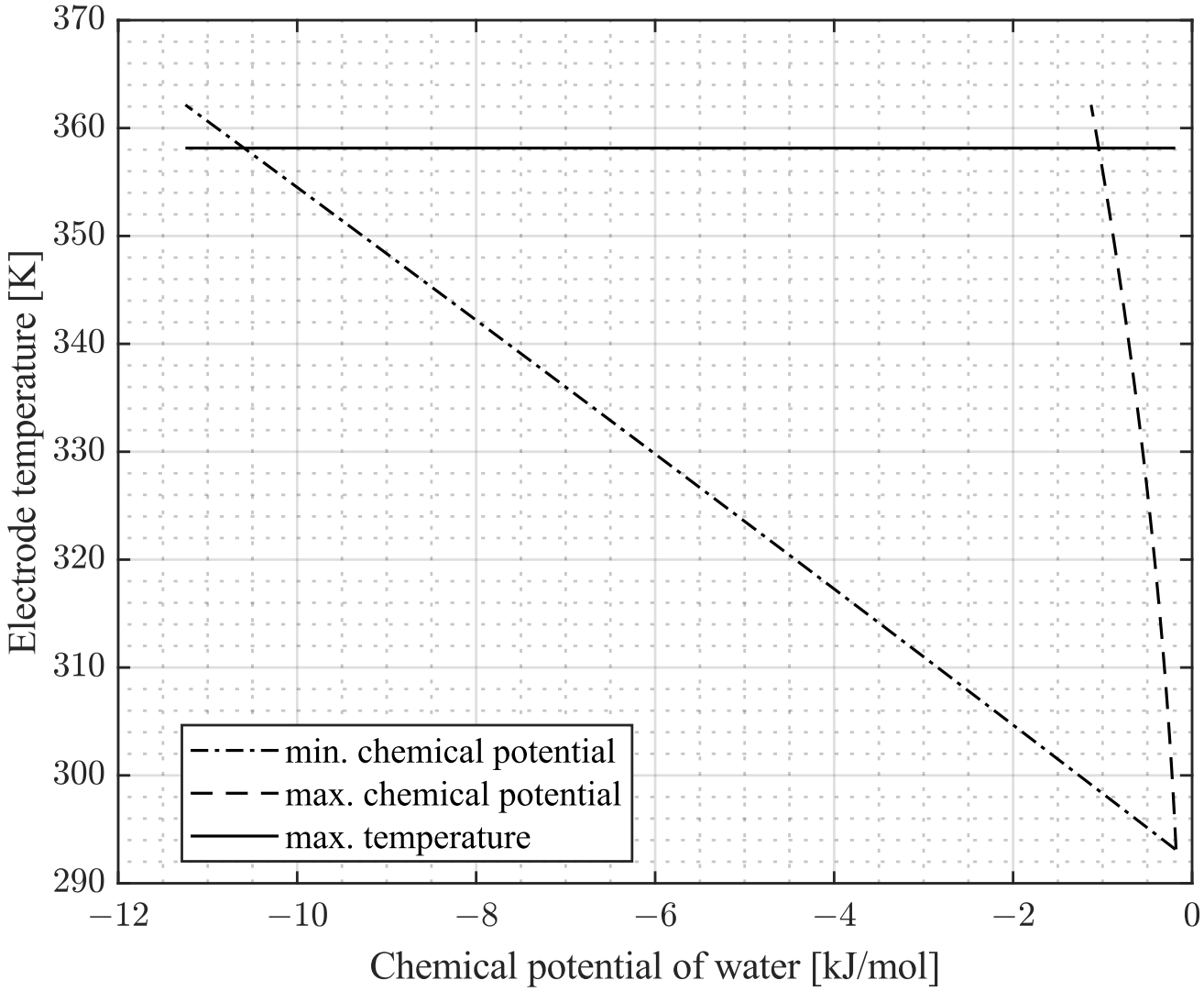

Figure 5. Possible range of measurement in terms of electrode temperatures and chemical potential of the water.

3.2. Calculation of the Temperature Profile and Water Distribution in the Sample Cell

According to Equation (6), the Nernst equation of the TGC needs knowledge of the gas composition and temperature at the membrane surface to determine the phenomenological coefficients. Since the implemented sensors only supply information on the gas composition at the inlet and temperatures in the flow field, a method to calculate these values at the membrane surface is required. For this reason, the model of a previous study [23] is adjusted so that the requested conditions at the membrane are inserted and the required conditions at the cell inlet are then calculated in order to be adjusted at the setup. The thermophysical fluid properties needed in the model are calculated using NIST REFPROP 10.0 [31] with default reference state. The model considers the heat and water transport through the membrane but neglects the gas crossover and uses classical transport coefficients as an approach for the phenomenological coefficients, leading to uncertainty in the regulated conditions at the membrane. A generic temperature profile calculated by the adjusted model is shown in Figure 6.

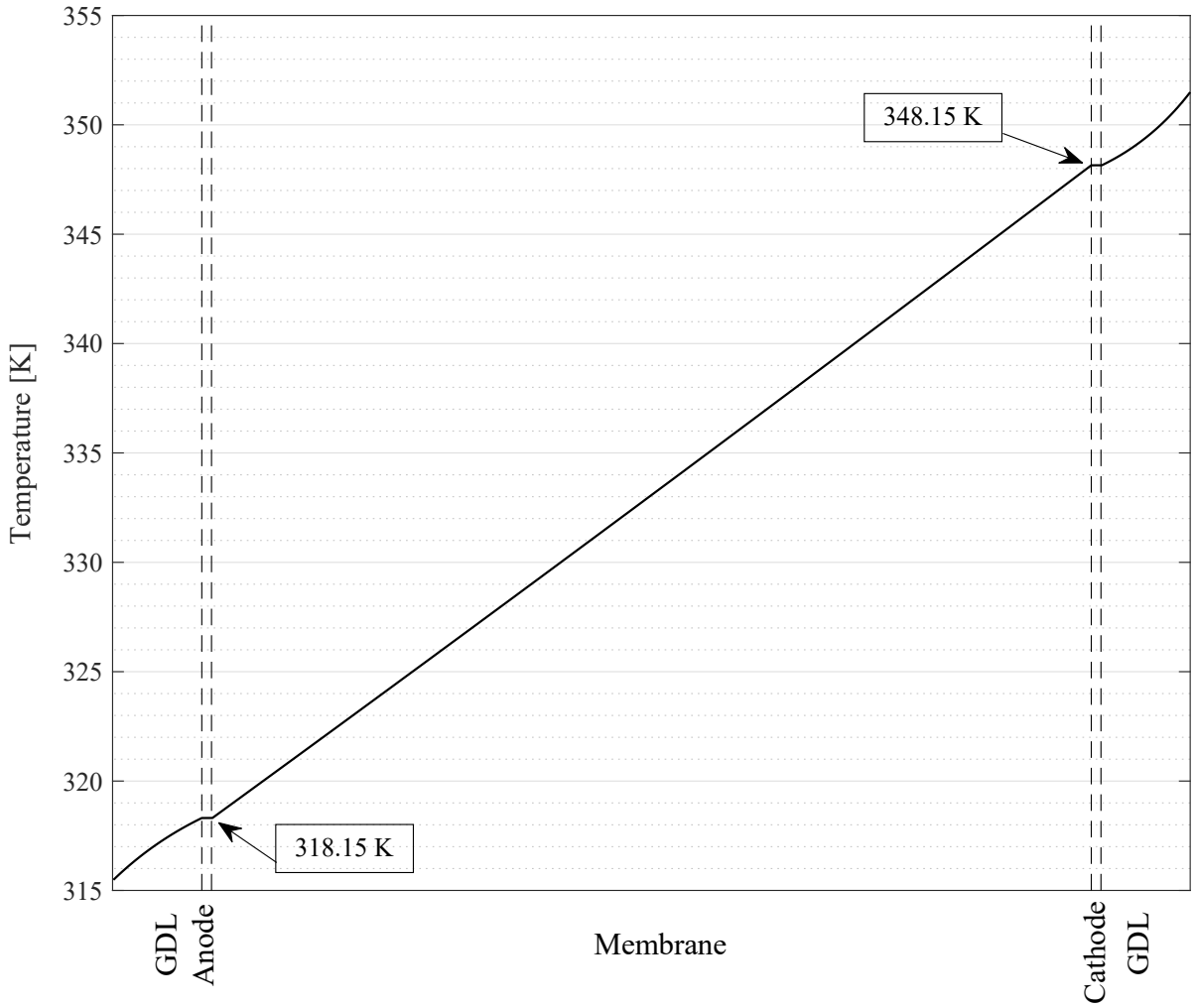

Figure 6. A generic temperature profile inside a test cell calculated by an adjusted model of [23].

3.3. Conditioning of the Membrane

Prior to setting up the sample cell, possible contaminants of the membrane were removed, and a reproducible test condition was set during a conditioning routine established by Møller-Holst [32]. The membranes were cleaned for 30 min in 5% H_2O_2 at 85 °C to remove organic contaminants, rinsed in purified water for 10 min at 70 °C afterwards, heated for 30 min in 0.05 M H_2SO_4 to eliminate metallic impurities, and finally rinsed several times with purified water at 70 °C to remove the remaining acid. To ensure steady-state conditions of the membranes' water content when recording the measurement data, the sample cell is fed humidified gas 20 h prior to the measurement. During this conditioning period of the membrane, filtered compressed air is used as the feed gas due to lower costs and availability. After switching to the required humidified gas stream (hydrogen/nitrogen/water), the test cell is kept at rest for another hour prior to recording data at the considered operation point.

3.4. Measurement of OCV

The OCV is measured for a variety of working conditions, i.e., gas composition and temperature of the electrodes. The hydrogen volume flow is set constant to 2.5 Nl/min while the water mass flow is adjusted between different measurements, leading to different chemical potentials of the water inside the electrolyte. As a first approach, the chemical potential of the liquid water inside the membrane is approximated by the chemical potential of the water vapor of the gas feed at the electrodes using NIST REFPROP 10.0 [31]. Due

to the phase change between a gaseous state of the water outside of the membrane and a liquid state inside the membrane, this assumption needs to be investigated in future work as the OCV is directly affected by the gradient of the chemical potential of the water inside the membrane (see Equation (12)).

3.5. Measurement of $L_{\phi\phi}$

For the measurements of $L_{\phi\phi}$, a gradient in temperature as well as a gradient in the chemical potential of the water across the membrane need to be avoided. This requirement implies a cell voltage of 0 V according to the Nernst equation (Equation (6)). After setting up the measurement conditions and reaching the cell voltage of 0 V, the electrochemical impedance spectroscopy (EIS) is carried out with an amplitude of 3 mA in a frequency spectrum from 1 Hz to 100 kHz. To determine the ohmic resistance of the test setup from the impedance spectra, the measured data is fitted to an equivalent circuit diagram. By subtracting all electrical contact resistances in the setup that were investigated prior to the EIS measurement, the phenomenological coefficient $L_{\phi\phi}$ is determined for various operation conditions; values are given in Table 3.

4. Results and Discussion

4.1. Open Circuit Voltage

All relevant features of the resulting OCV can be seen in Figure 7 as functions of the difference in the chemical potential of the water ($\Delta\mu^{w,m} = \mu^{w,c} - \mu^{w,a}$), the temperature gradient between the electrodes ($\Delta T^m = T^c - T^a$) and the mean membrane temperature T^m. The experimental data shows an increasing absolute value of the OCV and an increasing value of the difference in the chemical potential of the water. For negative $\Delta\mu^{w,m}$, an increasing ΔT^m is leading to higher OCVs, whereas for positive $\Delta\mu^{w,m}$ a reduction of ΔT^m results in higher absolute values of OCV. By comparing the values of a corresponding temperature difference at the same difference in the chemical potential, it can be seen that a larger mean membrane temperature results in a larger OCV. The measured OCV at a temperature difference of $\Delta T^m = 0$ K and a mean temperature of $T^m = 360$ K shows a significant impact of the chemical potential difference of water on the OCV of up to -40 mV. The maximum measured OCV at a chemical potential difference of $\Delta\mu^{w,m} = 0$ J/mol but a present temperature gradient of $\Delta T^m = 37$ K is less than 20 mV. Figure 7 indicates that the difference in the chemical potential of the water and the temperature, as well as the mean membrane temperature, have a significant impact on the OCV, which is in good accordance with the Nernst equation (Equation (6)).

By taking a closer look at the electrical potential difference across the membrane (Equation (12)) impacting the Nernst voltage (Equation (6)), this value can be divided into two terms. The first one (Equation (15)) includes the relation of the coefficients $L_{\phi q}$ and $L_{\phi\phi}$, which becomes multiplied with the ratio of the temperature difference across the membrane ΔT^m and the mean membrane temperature T^m:

$$-\frac{L_{\phi q}}{L_{\phi\phi}} \cdot \frac{\Delta T^m}{T^m}. \tag{15}$$

The second term (Equation (16)) contains the relation of the coefficients $L_{\phi w}$ and $L_{\phi\phi}$ and becomes multiplied with the difference in the chemical potential of the water across the membrane $\Delta\mu^{w,m}$:

$$-\frac{L_{\phi w}}{L_{\phi\phi}} \cdot \Delta\mu^{w,m}. \tag{16}$$

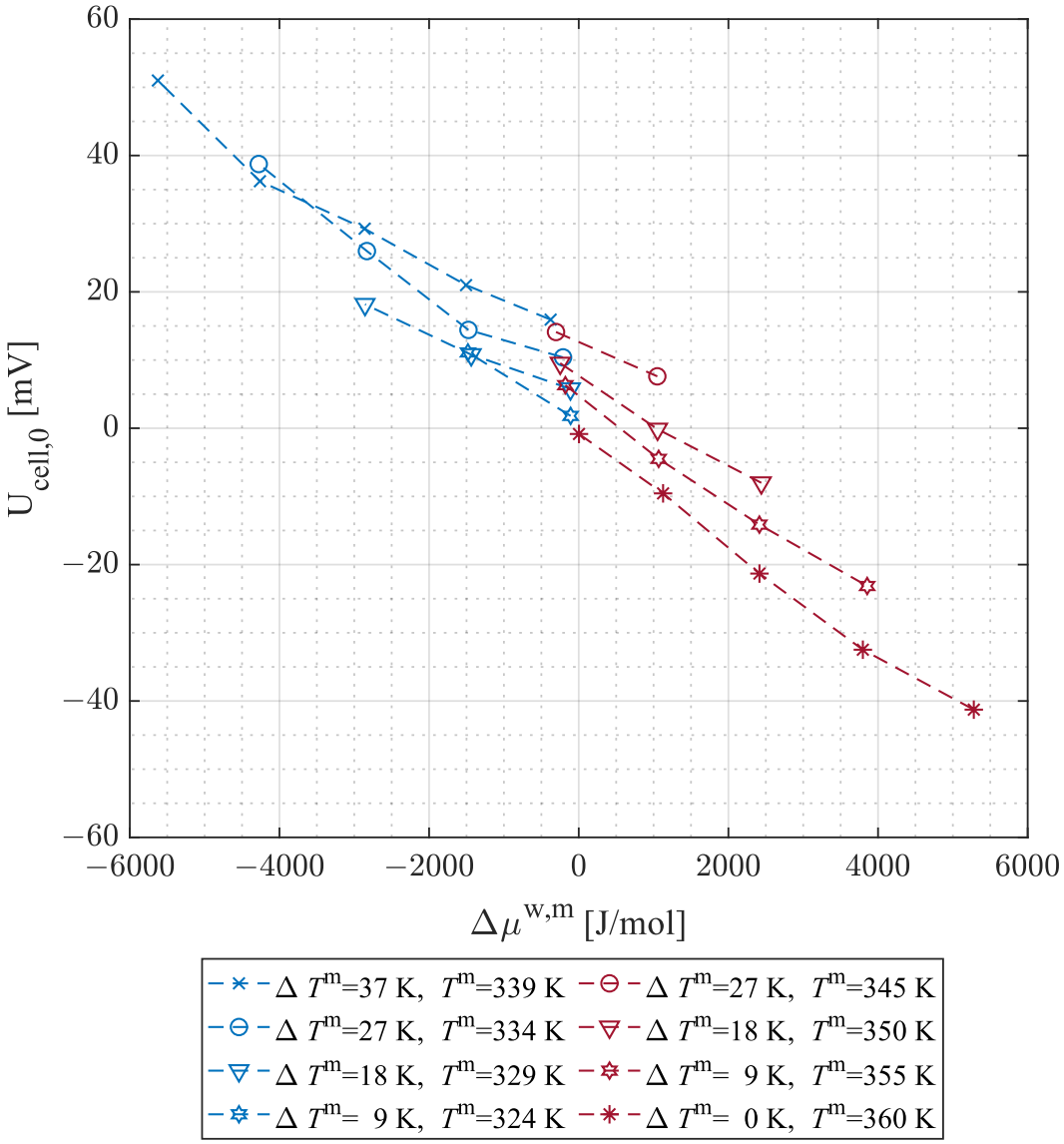

Figure 7. OCV depending on gradient in chemical potential of water $\Delta\mu^{w,m}$ for various T^m and ΔT^m.

Comparing different operating points of the cell with varied ΔT^m, T^m and $\Delta\mu^{w,m}$, as shown in Table 1, it can be observed that the impact on the electrical potential difference across the membrane for a similar $\Delta\mu^{w,m}$ but varying $\Delta T^m/T^m$ (OP 1, OP 2) is significantly lower than the effect of the $\Delta\mu^{w,m}$ for a constant $\Delta T^m/T^m$ (OP 2, OP 3). This could be an explanation for the larger impact of the $\Delta\mu^{w,m}$ on the OCV than of ΔT^m or T^m as already discussed when looking at Figure 7. To confirm this assumption, a closer look at the phenomenological coefficients in the membrane is needed.

Table 1. Calculated values of different terms contained in $\Delta\phi^m$ for different operating points (OP) of the cell i.e., varied ΔT^m, T^m and $\Delta\mu^{w,m}$.

OP	$U_{cell,0}$	$\Delta\phi^m$	ΔT^m	T^m	$\Delta T^m/T^m$	$\Delta\mu^{w,m}$
-	mV	mV	K	K	-	J/mol
1	−8.01	−30.1	18	350	0.051	2440
2	−14.13	−27.0	9	355	0.025	2414
3	−23.14	−36.9	9	355	0.025	3855

4.2. Impact of $\Delta\phi^m$ on the Open Circuit Voltage

When considering only the first term of the Nernst equation (Equation (6)) containing the difference in the chemical potential of the hydrogen between the electrodes and neglecting the difference in electrical potential across the membrane $\Delta\phi^{\mathrm{m}}$, one can calculate the OCV*:

$$\begin{aligned} \mathrm{OCV}^{*} &= \mathrm{OCV} - \Delta\phi^{\mathrm{m}} \\ &= \frac{G^{\theta}_{\mathrm{m},0,\mathrm{H_2}}(T^{\mathrm{a}})}{2\cdot F} - \frac{G^{\theta}_{\mathrm{m},0,\mathrm{H_2}}(T^{\mathrm{c}})}{2\cdot F} + \frac{R_{\mathrm{m}}\cdot T^{\mathrm{a}}}{2\cdot F}\cdot \ln\left(\frac{f^{\mathrm{a}}_{\mathrm{H_2}}\left(T^{\mathrm{a}},\, x^{\mathrm{a}}_{\mathrm{H_2}}\right)}{p^{\theta}}\right) \\ &\quad - \frac{R_{\mathrm{m}}\cdot T^{\mathrm{c}}}{2\cdot F}\cdot \ln\left(\frac{f^{\mathrm{c}}_{\mathrm{H_2}}\left(T^{\mathrm{c}},\, x^{\mathrm{c}}_{\mathrm{H_2}}\right)}{p^{\theta}}\right). \end{aligned} \tag{17}$$

The values of the calculated OCV* corresponding to the measured OCV, as presented in Figure 7, are presented in Figure 8 for $\Delta\mu^{\mathrm{w,m}} \geq -500\,\mathrm{J/mol}$ and in Figure 9 for $\Delta\mu^{\mathrm{w,m}} < 0\,\mathrm{J/mol}$. By comparing the data of the measured OCV and calculated OCV*, the significant impact of the difference in the electrical potential across the membrane $\Delta\phi^{\mathrm{m}}$ (gap between OCV and OCV* in the plot) is evident and intensifies with an increasing difference in the chemical potential of the water. While the measured OCV decreases for all temperature variations with a change in the difference in chemical potential of the water from negative ($\Delta\mu^{\mathrm{w,m}} < -6000\,\mathrm{J/mol}$) to positive values ($\Delta\mu^{\mathrm{w,m}} > 5000\,\mathrm{J/mol}$), the calculated OCV* shows an inverse dependence. The latter effect results from the rising difference in the chemical potential of the hydrogen between the anodic and cathodic electrodes, directly controlling the OCV*. Figure 8 shows the results of positive values of $\Delta\mu^{\mathrm{w,m}}$, which implies a higher cathodic value of the chemical potential of the water than the one at the anode. That means the gradient of temperature and chemical potential of the water appeal in the same direction. The values of the OCV are uniformly below the corresponding OCV*, which implies a negative value of $\Delta\phi^{\mathrm{m}}$ according to the Nernst equation (Equation (6)) for all data points. Since $\Delta T^{\mathrm{m}}/T^{\mathrm{m}}$ as well as $\Delta\mu^{\mathrm{w,m}}$ are positive values, and with the knowledge of positive $L_{\phi\phi}$ as discussed in a later section of this paper (see Figure 10), one can assume positive values for $L_{\phi\mathrm{q}}$ and $L_{\phi\mathrm{w}}$ in the considered scope of the chemical potential of water and temperatures. In the absence of gradients in temperature and chemical potential of the water over the membrane, the OCV is expected to be zero as well (see Equation (6)). Taking a look at this equilibrium condition shown in Figure 8, one can see an OCV slightly deviating from zero ($U_{\mathrm{cell},0}(\Delta T^{\mathrm{m}} = 0\,\mathrm{K},\ \Delta\mu^{\mathrm{w,m}} = 0\,\mathrm{J/mol},\ T^{\mathrm{m}} = 360\,\mathrm{K}) = -0.84$ mV). This inconsistency could be explained by a small variance in the positions of the thermoelements implemented in the flow field (see Figure 4), of which the temperature is used as the controlled variable for the electrode temperatures. As a result, a slight temperature gradient across the membrane could occur, although the measured gradient is zero. Due to the dependency of the chemical potential of the water on the temperature, the impact on the OCV could be even higher.

Figure 9 presents the values of OCV and OCV* for negative differences in the chemical potential of the water between anode and cathode, meaning that this gradient is now counteracting the gradient in the electrode temperatures. For slightly negative $\Delta\mu^{\mathrm{w,m}}$ close to 0 J/mol the values of OCV exceed the ones of OCV*, leading to a negative value of $\Delta\phi^{\mathrm{m}}$ and therefore showing a similar behavior as for positive $\Delta\mu^{\mathrm{w,m}}$. As the $\Delta\mu^{\mathrm{w,m}}$ is negative, either the value of Equation (15) needs to exceed the one of Equation (16), which is only possible if $L_{\phi\mathrm{q}} \gg L_{\phi\mathrm{w}}$ according to Table 1, or the phenomenological coefficients $L_{\phi\mathrm{w}}$ must have a negative sign to fulfill this condition.

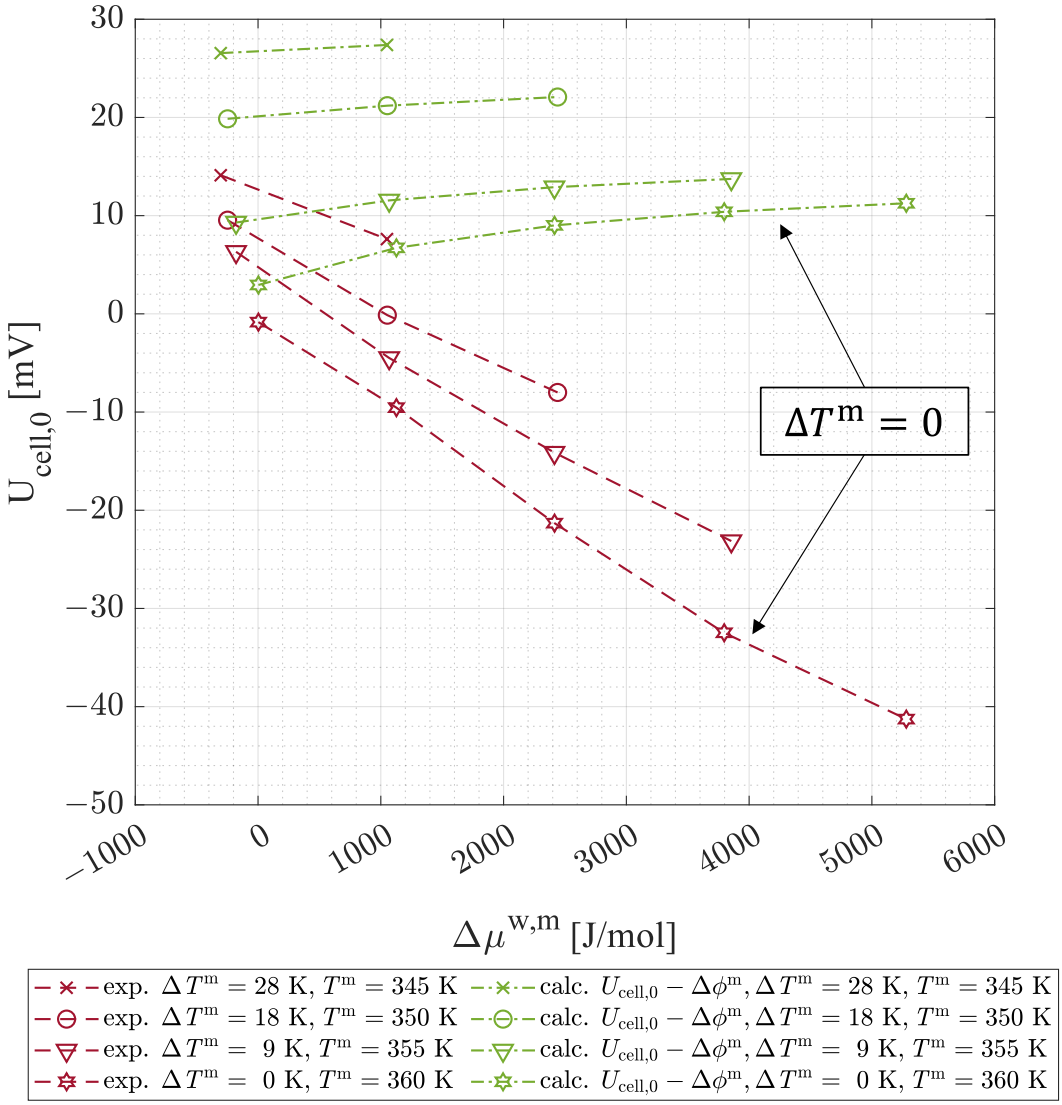

Figure 8. Measured OVC and calculated OCV* using the Nernst equation **without** $\Delta\phi^m$ for $\Delta\mu^{w,m} \geq -500$ J/mol .

Considering an increase in the negative differences of the chemical potential of the water, one can see an intersection of the measured OCV and the calculated OCV*, which moves to greater negative values of $\Delta\mu^{w,m}$ as the value of $\Delta T^m/T^m$ increases. These points of intersection (IP), which are presented in Table 2, imply a non-existent difference in electrical potential across the membrane as a result of the gradients across the membrane annulling each other in accordance with Equation (12). For $\Delta\phi^m = 0$ mV and rearranging Equation (12), one can calculate the ratio of $L_{\phi q}$ and $L_{\phi w}$, which enables a first estimate of the impact of the different gradients on the OCV:

$$\frac{L_{\phi q}}{L_{\phi w}} = -\frac{T^m \cdot \Delta\mu^{w,m}}{\Delta T^m}. \tag{18}$$

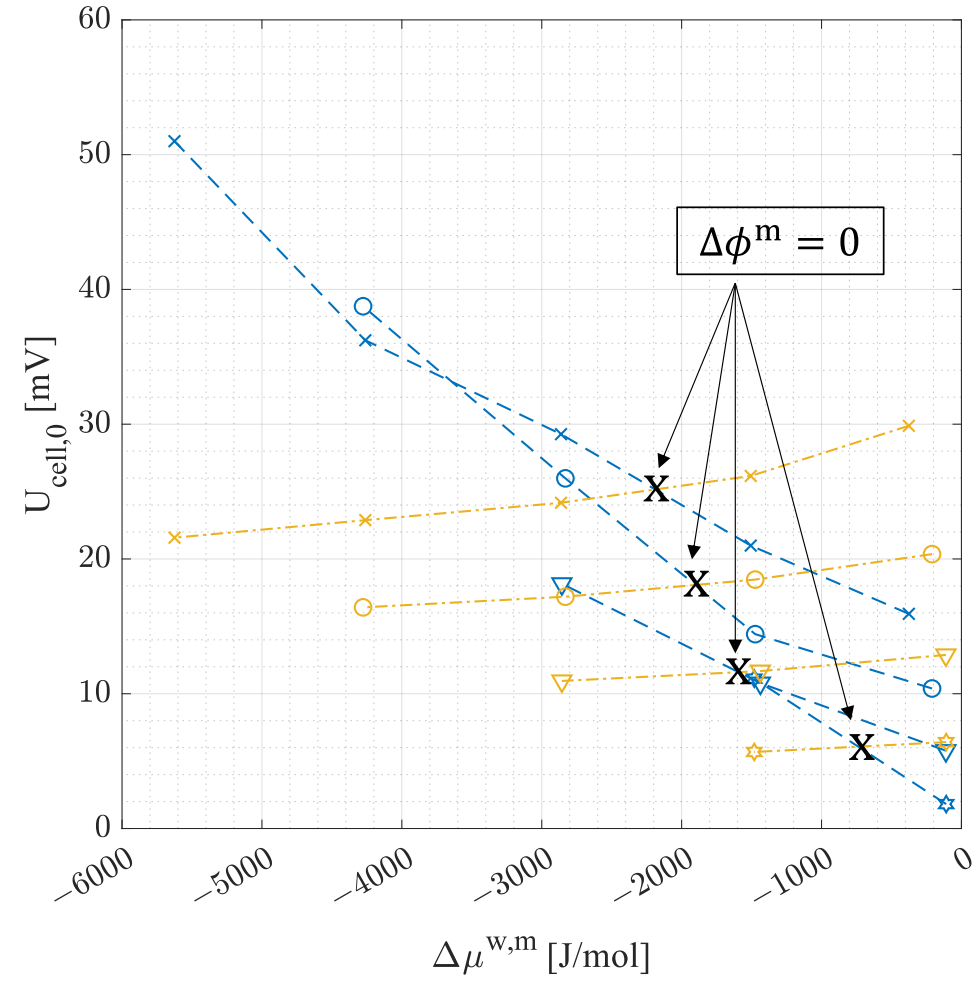

Figure 9. Measured OVC and calculated OCV* using the Nernst equation **<u>without</u>** $\Delta\phi^{\mathrm{m}}$ for $\Delta\mu^{\mathrm{w,m}} < 0\,\mathrm{J/mol}$.

Table 2. Point of intersection of OCV and OCV* for different operating conditions displayed in Figure 9.

IP	ΔT^m	T^m	$\Delta T^m/T^m$	$\Delta\mu^{w,m}$	$L_{\phi q}/L_{\phi w}$
-	K	K	-	J/mol	10^3 J/mol
1	9	324	0.028	−1304	46.8
2	18	329	0.055	−1796	32.8
3	27	334	0.081	−2286	28.3
4	37	339	0.11	−2601	23.8

By taking a closer look at the calculated values of $L_{\phi\mathrm{q}}/L_{\phi\mathrm{w}}$ in Table 2, one can see the values of $L_{\phi\mathrm{q}}$ exceeding those of $L_{\phi\mathrm{w}}$ on the order of 10^4. This shows a significantly larger impact of the temperature difference on the ionic flux in the membrane than the chemical potential of the water. Due to the restricted range of temperatures for operating the cell, the possible differences in temperature are quite small. Apparently, this leads to a more significant impact of the difference in chemical potential in water, which may

vary in a range of 10^3 and higher, as already discussed based on the data points in Table 1. The comparison of the different IPs shows a reduction of the ratio of $L_{\phi q}/L_{\phi w}$ with an increasing $\Delta T^m/T^m$ and $\Delta\mu^{w,m}$ meaning a comparatively greater increase of $L_{\phi w}$ than $L_{\phi q}$ and therefore a growing impact of the difference in chemical potential of the water on the $\Delta\phi^m$. For values of $\Delta\mu^{w,m}$ below the IP-related differences in the chemical potential of the water, the OCV exceeds the OCV*, leading to a positive value of $\Delta\phi^m$. This can be accomplished either by a negative value of $L_{\phi q}$ or a higher impact of the negative value of Equation (16) than the value of Equation (15), whereas the latter is more likely to be true according to the results presented in Table 2. The determination of the coefficients $L_{\phi q}$ and $L_{\phi w}$ could give some definite indication of this assumption.

4.3. Phenomenological Coefficient $L_{\phi\phi}$

Figure 10 presents the phenomenological coefficient $L_{\phi\phi}$ as determined using the EIS (see Section 3.5) in dependence on the membrane temperature ($\Delta T^m = 0$, $T^c = T^a = T^m$) and the chemical potential of the water in the membrane ($\Delta\mu^{w,m} = 0$, $\mu^{w,c} = \mu^{w,a} = \mu^{w,m}$) (solid lines). All gradients except the one in electrical potential across the membrane are suppressed. The results show an increasing $L_{\phi\phi}$ with a growth in the temperature and in the chemical potential of the membrane water. The impact of the increasing temperature is more significant for higher values of the chemical potential of the water. The values of $L_{\phi\phi}$ are given in Table 3. Some values of $L_{\phi\phi}$ are missing due to the restricted range of measurement (see Figure 5).

Table 3. $L_{\phi\phi}$ for different chemical potentials of the water and membrane temperatures in S K/cm.

Chem. Pot. of Water $\mu^{w,m}$ [J/mol]	**Membrane Temperature T [K]**				
	313.15	**323.15**	**333.15**	**343.15**	**353.15**
−1038	5.91	8.70	15.19	35.45	42.17
−1539	6.50	7.72	9.48	16.67	22.86
−2539	3.75	4.44	5.69	6.30	9.66
−3354	-	2.34	3.16	4.04	5.46
−5538	-	-	1.15	1.43	2.06
−8040	-	-	-	0.39	0.67

There is a conceptual difference between the phenomenological coefficients L_{ij} and the classical coefficients like the ionic conductivity κ^m, the heat conductivity k or the diffusion coefficient D_{ij}. The L_{ij} arise from the multicausal approach and designate a transport mechanism solely by one gradient. The monocausal transport mechanisms are typically effective since other gradients are unknown. To compare the measured $L_{\phi\phi}$ with the classical transport coefficient κ^m for validation purposes, one needs to translate the chemical potential of the water into the water content in the membrane λ^w, as this is included in Equation (14). A sorption isotherm [26] is commonly used as an approach to describe the dependency of the water content of the membrane on the activity and temperature of the water inside the membrane. Therefore, the chemical potential of the water shows a growth in the water content with increasing chemical potential and temperature. Taking this relation into account and applying it to the measured results, a comparison with the experimental values of $L_{\phi\phi}$ and the calculated values of κ^m using Equations (13) and (14) shows a somewhat similar behavior (structured lines in Figure 10), indicating the credibility of the measured data, which is also in good accordance with the other literature [33]. When comparing the absolute values of the measured and calculated $L_{\phi\phi}$ as presented in Figure 10, there are smaller values of the experimental data for low $\mu^{w,m}$ and T^m than for the calculated data, which changes with increasing T^m for high $\mu^{w,m}$. As the test cell used in our work consists of a stacked layer of six membranes, internal contact resistances occur, which can lead to a decreasing ionic conductivity of the overall test cell. In addition, some inconsistency in the solid electrolyte, for example, air gaps between membranes, could be a reason for the deviations. A rising T^m and $\mu^{w,m}$ lead to an increasing water content

of the membrane λ^{w}. For a high λ^{w}, water could accumulate inside the membrane and between the contact areas, leading to the formation of water channels that promote ion transport and therefore increase the ionic conductivity of the membrane. To prove this assumption, experimental investigations on $L_{\phi\phi}$ with varying amounts of membranes will be conducted in future work.

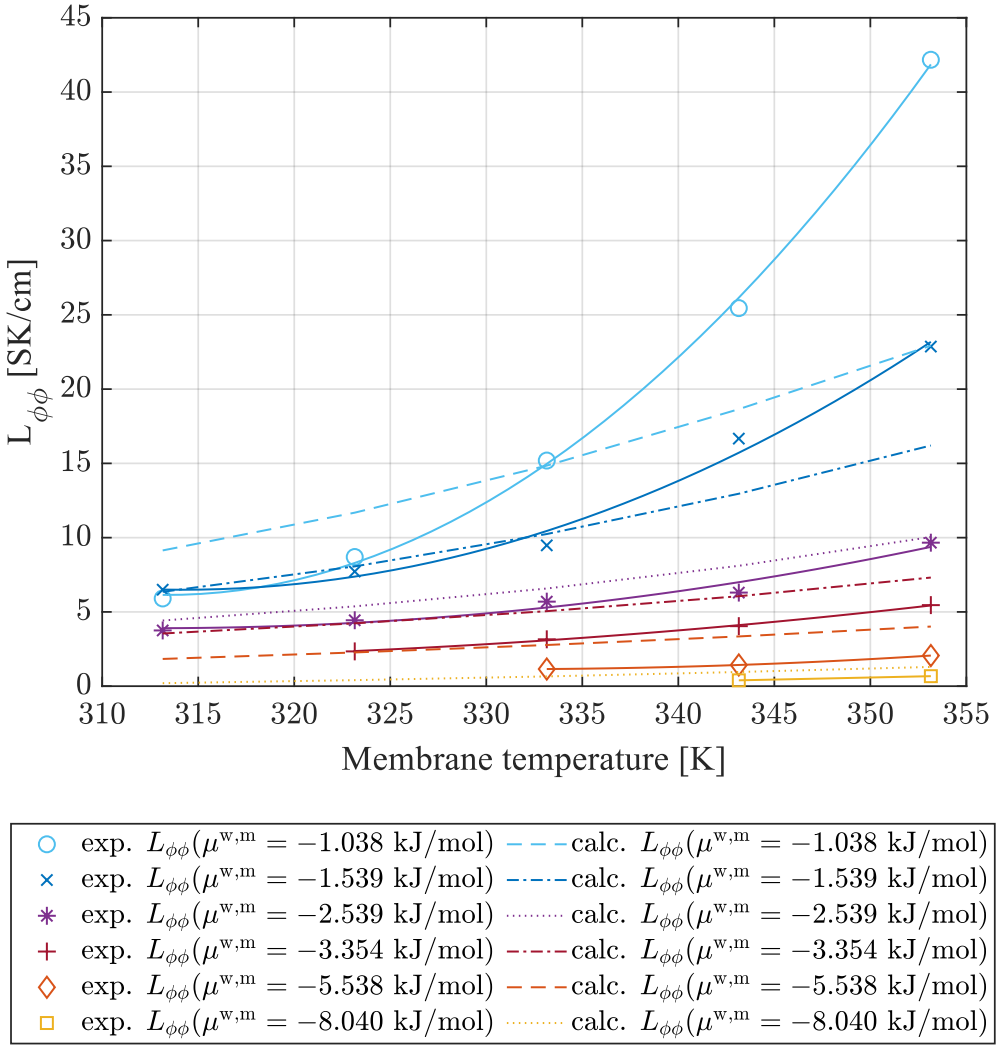

Figure 10. Exp. (solid lines) and calc. (structured lines) $L_{\phi\phi}$ in dependency on the membrane temperature and chemical potential of the water inside the electrolyte ($\Delta T^{m} = 0$ K, $\Delta\mu^{w,m} = 0$ J/mol).

5. Conclusions

The experiments were carried out under a wide variety of working conditions, i.e., temperatures and gas compositions of the electrodes. The results show an increasing absolute OCV with increasing chemical potential of the water, as well as an increasing temperature difference and an increasing mean membrane temperature. The measured effect of a difference in the chemical potential of the water on the OCV is clearly higher than the impact of the temperature. The comparison of the phenomenological coefficients $L_{\phi q}$ and $L_{\phi w}$ representing the solely relation between the temperature gradient and the ionic flux as well as the gradient in the chemical potential of the water and the ionic flux, respectively, indicate a, in an order of 10^4 higher value of the $L_{\phi q}$ discounting the previous assumption. The apparently higher impact of the chemical potential of the water is due to the restricted range of temperature of the test setup being on the order of 10^3 smaller than the difference in the chemical potential of the water. As the gradient in the chemical potential of the

water $\Delta\mu^{w,m}$ is of predominant importance to the functionality of the TGC, the current calculation of these values shall be recalled and replaced by a more accurate one. When taking a closer look at the Nernst equation for different working conditions, one can see a significant impact of the electric potential difference arising across the electrolyte. To be able to characterize this effect, the coupled transport phenomena taking place in the electrolyte need to be investigated by measuring the coupling coefficients, starting with $L_{\phi\phi}$. By comparing the results from this phenomenological coefficient with the ionic conductivity as a well-examined classical transport coefficient, similar characteristics regarding the dependency on temperature and chemical potential of the water can be observed, showing a first validation of the results. When measuring the other two phenomenological coefficients $L_{\phi q}$ and $L_{\phi w}$ impacting the OCV in future work, the various effects on the OVC can be analyzed in more detail and can be separated into their original causes. The knowledge of these coefficients, in combination with the measurement of gradients occurring across the electrolyte, enables the determination of the local entropy production rate. As the latter is directly connected with the heat production, it can enable the optimization of the performance of a TGC needed prior to its commercial use.

Author Contributions: Conceptualization, M.W. and S.K.; methodology, M.W. and N.-E.R.; software, M.W. and N.-E.R.; validation, M.W.; formal analysis, M.W.; investigation, M.W. and N.-E.R.; writing—original draft preparation, M.W.; visualization, M.W.; writing—review and editing, supervision, project administration and funding acquisition, S.K. All authors have read and agreed to the published version of the manuscript.

Funding: The authors gratefully acknowledge the financial support by the Deutsche Forschungsgemeinschaft (project no. 449554201).

Data Availability Statement: The data presented in this study are available on request from the corresponding author. The data are not publicly available due to ongoing research.

Conflicts of Interest: The authors declare no conflict of interest.

Abbreviations

The following abbreviations are used in this manuscript:

CEM	Controlled Evaporation Mixing
EIS	Electrochemical Impedance Spectroscopy
EMF	Electromotive Force
FC	Fuel Cell
FF	Flow Field
HFR	High Frequency Resistance
MEA	Membrane Electrode Assembly
MFC	Mass Flow Controller
NET	Non-Equilibrium Thermodynamics
OCV	Open Circuit Voltage
PEM	Polymer Electrolyte Membrane
TEG	Thermoelectric Generator
TGC	Thermogalvanic Cell
Roman symbols	
D	diffusion coefficient $\left[\mathrm{m^2\ s^{-1}}\right]$
f	fugacity [Pa]
F	Faraday constant [A s $\mathrm{mol^{-1}}$]
j	current density [A $\mathrm{m^{-2}}$]
J_i	molar flux density [mol $\mathrm{s^{-1}\ m^{-2}}$]
J'_q	measurable heat flux density [W $\mathrm{m^{-2}}$]
J_w	molar water flux density [mol $\mathrm{s^{-1}\ m^{-2}}$]
k	thermal conductivity [W $\mathrm{m^{-1}\ K^{-1}}$]
L_{ij}	phenomenological coefficient [-]
$L_{\phi\phi}$	phenomenological coefficient $\left[\mathrm{S\ K\ cm^{-1}}\right]$

$L_{\phi q}$	phenomenological coefficient [A K cm^{-1}]
$L_{\phi w}$	phenomenological coefficient [K mo lV^{-1} s^{-1} cm^{-1}]
r	electrical resistance [Ω]
R_m	universal gas constant [J mol^{-1} K^{-1}]
$\dot{s}_{v,irr}$	volumetric entropy production rate [J K^{-1} mol^{-1}]
$t^{w,m}$	water transference number [-]
$U_{cell,0}$	open circuit voltage [V]
x	molar fraction [-]
X	intrinsic corresponding force [-]
Greek symbols	
κ	electrical conductivity [S cm^{-1}]
λ	water content [-]
μ	chemical potential [J mol^{-1}]
π	Pelter coefficient [J mol^{-1}]
ϕ	electrical potential [V]
Subscripts	
a	anode
c	cathode
m	Membrane
max	maximum
w	water

References

1. Mamur, H.; Dilmaç, Ö.F.; Begum, J.; Bhuiyan, M.R.A. Thermoelectric generators act as renewable energy sources. *Clean. Mater.* **2021**, *2*, 100030. [CrossRef]
2. Ismail, B.; Ahmed, W. Thermoelectric Power Generation Using Waste-Heat Energy as an Alternative Green Technology. *EENG* **2009**, *2*, 27–39. [CrossRef]
3. Zulkepli, N.; Yunas, J.; Mohamed, M.A.; Hamzah, A.A. Review of Thermoelectric Generators at Low Operating Temperatures: Working Principles and Materials. *Micromachines* **2021**, *12*, 734. [CrossRef] [PubMed]
4. Duan, J.; Feng, G.; Yu, B.; Li, J.; Chen, M.; Yang, P.; Feng, J.; Liu, K.; Zhou, J. Aqueous thermogalvanic cells with a high Seebeck coefficient for low-grade heat harvest. *Nat. Commun.* **2018**, *9*, 5146. [CrossRef] [PubMed]
5. Abraham, T.J.; MacFarlane, D.R.; Pringle, J.M. High Seebeck coefficient redox ionic liquid electrolytes for thermal energy harvesting. *Energy Environ. Sci.* **2013**, *6*, 2639. [CrossRef]
6. Dupont, M.F.; MacFarlane, D.R.; Pringle, J.M. Thermo-electrochemical cells for waste heat harvesting-progress and perspectives. *Chem. Commun.* **2017**, *53*, 6288–6302. [CrossRef]
7. Lee, S.W.; Yang, Y.; Lee, H.-W.; Ghasemi, H.; Kraemer, D.; Chen, G.; Cui, Y. An electrochemical system for efficiently harvesting low-grade heat energy. *Nat. Commun.* **2014**, *5*, 3942. [CrossRef]
8. Zhu, X.; Rahimi, M.; Gorski, C.A.; Logan, B. A Thermally-Regenerative Ammonia-Based Flow Battery for Electrical Energy Recovery from Waste Heat. *ChemSusChem* **2016**, *9*, 873–879. [CrossRef]
9. Bonetti, M.; Nakamae, S.; Roger, M.; Guenoun, P. Huge Seebeck coefficients in nonaqueous electrolytes. *J. Chem. Phys.* **2011**, *134*, 114513. [CrossRef]
10. Marquardt, T.; Kube, J.; Radici, P.; Kabelac, S. Experimental investigation of a thermocell with proton exchange membrane and hydrogen electrodes. *Int. J. Hydrogen Energy* **2020**, *45*, 12680–12690. [CrossRef]
11. Burmistrov, I.; Khanna, R.; Gorshkov, N.; Kiselev, N.; Artyukhov, D.; Boychenko, E.; Yudin, A.; Konyukhov, Y.; Kravchenko, M.; Gorokhovsky, A.; et al. Advances in Thermo-Electrochemical (TEC) Cell Performances for Harvesting Low-Grade Heat Energy: A Review. *Sustainability* **2022**, *14*, 9483. [CrossRef]
12. Weng, G.-M.; Li, C.-Y.V.; Chan, K.-Y. Hydrogen battery using neutralization energy. *Nano Energy* **2018**, *53*, 240–244. [CrossRef]
13. Ma, H.; Wang, X.; Peng, Y.; Peng, H.; Hu, M.; Xiao, L.; Wang, G.; Lu, J.; Zhuang, L. Powerful Thermogalvanic Cells Based on a Reversible Hydrogen Electrode and Gas-Containing Electrolytes. *ACS Energy Lett.* **2019**, *4*, 1810–1815. [CrossRef]
14. Loktionov, P.; Konev, D.; Antipov, A. Hydrogen-assisted neutralization flow battery with high power and energy densities. *J. Power Sources* **2023**, *564*, 232818. [CrossRef]
15. Wijeratne, K. *Conducting Polymer Electrodes for Thermogalvanic Cells*, 1st ed.; Linkopings Universitet: Linköping, Switzerland; ProQuest: Ann Arbor, MI, USA, 2018.
16. Kjelstrup, S.; Vie, P.; Akyalcin, L.; Zefaniya, P.; Pharoah, J.G.; Burheim, O.S. The Seebeck coefficient and the Peltier effect in a polymer electrolyte membrane cell with two hydrogen electrodes. *Electrochim. Acta* **2013**, *99*, 166–175. [CrossRef]
17. Yang, L.; Sun, H.; Wang, S.; Jiang, L.; Sun, G. A solid state thermogalvanic cell harvesting low-grade thermal energy. *Int. J. Hydrogen Energy* **2017**, *42*, 25877–25881. [CrossRef]

18. O'Hayre, R.P.; Cha, S.-W.; Colella, W.G.; Prinz, F.B. *Fuel Cell Fundamentals*; Wiley: Hoboken, NJ, USA, 2016.
19. Onsager, L. Reciprocal Relations in Irreversible Processes I. *Phys. Rev.* **1931**, *37*, 405–426. [CrossRef]
20. Onsager, L. Reciprocal Relations in Irreversible Processes II. *Phys. Rev.* **1931**, *38*, 2265–2279. [CrossRef]
21. Kjelstrup, S.; Bedeaux, D.; Johannessen, E.; Gross, J. (Eds.) *Non-Equilibrium Thermodynamics for Engineers*; World Scientific: Singapore, 2017.
22. Kjelstrup, S.; Røsjorde, A. Local and total entropy production and heat and water fluxes in a one-dimensional polymer electrolyte fuel cell. *J. Phys. Chem. B* **2005**, *109*, 9020–9033. [CrossRef]
23. Marquardt, T.; Huerta, G.V.; Kabelac, S. Modeling a thermocell with proton exchange membrane and hydrogen electrodes. *Int. J. Hydrogen Energy* **2018**, *43*, 19841–19850. [CrossRef]
24. Sone, Y.; Ekdunge, P.; Simonsson, D. Proton Conductivity of Nafion 117 as Measured by a Four-Electrode AC Impedance Method. *J. Electrochem. Soc.* **1996**, *143*, 1254–1259. [CrossRef]
25. Liu, L.; Chen, W.; Li, Y. An overview of the proton conductivity of nafion membranes through a statistical analysis. *J. Membr. Sci.* **2016**, *504*, 1–9. [CrossRef]
26. Springer, T.E.; Zawodzinski, T.A.; Gottesfeld, S. Polymer Electrolyte Fuel Cell Model. *J. Electrochem. Soc.* **1991**, *138*, 2334–2342. [CrossRef]
27. Sauermoser, M.; Kjelstrup, S.; Pollet, B.G. The Impact of Peltier and Dufour Coefficients on Heat Fluxes and Temperature Profiles in the Polymer Electrolyte Fuel Cells. *J. Electrochem. Soc.* **2020**, *167*, 144503. [CrossRef]
28. Gasik, M. Materials for Fuel Cells. CRC Press: Cambridge, UK; Woodhead Publishing Ltd.: Boca Raton, FL, USA, 2008.
29. Daud, W.; Rosli, R.E.; Majlan, E.H.; Hamid, S.; Mohamed, R.; Husaini, T. PEM fuel cell system control: A review. *Renew. Energy* **2017**, *113*, 620–638. [CrossRef]
30. Barbir, F. *PEM Fuel Cells: Theory and Practice*; Elsevier: Amsterdam, The Netherlands, 2013.
31. Lemmon, E.W.; Bell, I.H.; Huber, M.L.; McLinden, M.O. *NIST Standard Reference Database 23: Reference Fluid Thermodynamic and Transport Properties-REFPROP*; National Institute of Standards and Technology: Gaithersburg, MD, USA, 2018.
32. Moeller-Holst, S. *Solid Polymer Fuel Cells. Electrode and Membrane Performance Studies*; Norges Teknisk-Naturvitenskapelige Universitet: Trondheim, Norway, 1996.
33. Kusoglu, A.; Weber, A.Z. New Insights into Perfluorinated Sulfonic-Acid Ionomers. *Chem. Rev.* **2017**, *117*, 987–1104. [CrossRef]